Twining ZnO nanoparticles to nanorods with control growth and size-shape dependent interactions with cancer cells: Role of physical properties and cell inhibition

Vijay Bhooshan Kumar, Pradip Paik*

School of Engineering Sciences and Technology, University of Hyderabad, Hyderabad, Telangana, India

*Corresponding author, Tel: (+91)-(040) 2313 4457; E-mail: pradip.paik@gmail.com, ppse@uohyd.ernet.in, paik@uohyd.ac.in

Received: 09 February 2016, Revised: 30 November 2016 and Accepted: 12 December 2016

DOI: 10.5185/amlett.2017.6474
www.vbripress.com/aml

Abstract

In this work, we reported the control size and shape dependent cellular interactions of ZnO nanoparticles ranging from tiny nanodisks to nanorods, with carcinoma cells. These particles were synthesized through the wet chemical synthesis approach. Size and shape of the ZnO nanoparticles were tuned by varying the concentration of Igapal CO50. Size and shape dependent interactions were investigated with human carcinoma cells (K562, a Leukaemia Cancer Cells) without attaching any anticancer drugs and the results manifest that the size, shape and physical properties of ZnO nanoparticles are preferentially the critical factors in interactions and killing the cancer cells when no anticancer drugs were used. ZnO nanoparticles are used of aspect ratio from 1.3 to 5.5. Interaction and killing of carcinoma cells depend on the extent of defects and on the electro paramagnetic behavior of the ZnO nanoparticles. Further, Raman and EPR studies revealed that the size dependent phonon localization of oxygen defects of ZnO control the formation of singlet oxygen on interactions with cancer cells and regulate the anticancer effects of ZnO nanoparticles even in the absence of drugs. ZnO NPs with low aspect ratio is more vigorous in killing the carcinoma cells.

Keywords: ZnO nanoparticles, nanorodes, carcinoma cells, cell inhibition.

Introduction

Over the last few decades, Zinc oxide (ZnO) nanoparticles have been used for designing semiconductor device due to their specific properties, such as n-type II–VI semiconducting nature, wide band gap (3.37 eV), large excitation binding energy (60 meV), and promising piezoelectric behavior **[1].** Furthermore, they have potential uses in biotechnology due to their relatively high bio-compatibility compared to the other metal oxide nanoparticles **[2–7].** ZnO nanoparticles can be synthesized to have different morphologies, such as sheets, tubes, flowers, and rods, depending on the synthesis approach having difference in optical, electrical, and thermoelectric properties **[8–10]**. Properties of ZnO NPs are affected by the conditions applied during its synthesis, micro wave, UV-Vis light, temperature, solvents used, and reaction temperature and heating rate. The synthesis approach also impact on the shape, size and morphologies **[11–13]**. Chemical synthesis routes of ZnO can exhibit differences in surface chemical structure and defects. Sirelkhatim *et al.* recently reported the preferential cytotoxicity of ZnO nanoparticle, ZnO disks (20 nm) and pellets (40 nm) to evaluate ROS-mediated apoptosis cell death and cell cycle arrest to HeLa cells [**14**]. Cai *et al.* informed ZnO quantum dots-based pH responsive drug delivery platform for intracellular controlled release of drugs [15]. However, ZnO nanoparticles that undergone surface modification can have differences in interactions and responses with living organism, such as with micro-organisms (e.g. bacteria) **[16]** and other living cells such as T-cells [4], cancer cells **[4,6,7]** etc. In all earlier works the toxicity, shape, size and morphologies of the ZnO NPs used are reported based on the different synthesis routes. It is worth mentioning that the different synthesis routes produce differences in structures. However, by changing a single parameter during the synthesis will have better control on the size, shape, morphology, physical properties and interactions with living cells are of great interest with regards to tune the biological activities and applications in the same field. This study especially offers a better inspect in order to get a better understanding of the growth of ZnO NPs and their interactions with cancer cells.

In this work, we have focused on the facile synthesis of various shapes of ZnO nanoparticles during chemical synthesis routes by varying the concentration of Igapal CO50 only used in this study. ZnO NPs are of disk shaped nanoparticles to nanorods (growth in z-direction) with

different aspect ratio, self-assembled dandelion nanocapsules and triangular ZnO nanoparticles are taken into consideration for this study. Finally, we have studied the interactions of these ZnO particles with human carcinoma cells *in-vitro* and correlated the cytocompatibility with their physical properties and defects with size and shape. The results reveal that the detailed study of this work impacts on the properties of ZnO nanoparticles and biological activities, which further will aid to the large biomaterials community to consider these materials in various possible biomedical applications

Experimental

Synthesis of ZnO nanomaterials

The chemically modified routes were followed to obtain the ZnO nanoparticles. In six separate beakers in each, 5g of zinc acetate (99·98% pure, Sigma-Aldrich) was dissolved in 50 mL of distilled water. 1mL to 0.05mL surfactant (Igapal CO 50) was added drop wise to the aqueous $Zn(Ac)_2$ solution under constant stirring overnight. While taking precursor separately in 6 different beakers, the surfactant was added in measures of 1000 µL, 750 µL, 500 µL, 250 µL, 100 µL and 50 µL, respectively. For slow but progressive reactions, the beakers were covered with aluminium foil and kept onto a hot plate with continuous vigorous stirring with 1000 rpm and at 80 ºC for 24 hours. As white precipitate products were formed, they were separated through filtration and then subjected to hot air oven drying at 120 ºC for 2 hrs. Knowing that surfactant has a degradation temperature ~300 ºC, and in order to remove unwanted impurities along with the surfactant, each of the products were calcined at 500 ºC for 4 hrs to get the pure ZnO nanostructures. The samples will be referred to by the following names **(Table 1).**

Table 1. ZnO nanoparticles with different, size, shape and aspect ratios synthesized and used in this study.

Samples ID	Surfactant conc. (µL)	Shape	Aspect ratio#
S1	1000	Only long rods (100%)	~5.7
S2	750	Irregular spherical NPs + moderately rods with medium length (50:50_	~4.1
S3	500	Irregular spherical NPs (mostly) + rods with less amount	~3.8
S4	250	Irregular spherical NPs + rods with low aspect ratio	~3.0
S5	100	Irregular NPs	~1.8
S6	50	Regular spherical particles	~1.3

#on the basis of (microscopy analysis)

Characterization of materials

To find out the solid state structural and surface morphological properties of sample S1-S6, X-ray diffraction (XRD) measurements were performed on a Bruker D8 Advance X-ray diffractometer using Cu-Kα radiation operating at 40kV/30mA with a 0.02 step size and a 1s step. The synthesized nanoscale powders were poured in IPA (isopropanol) with very low concentration and measured the absorption spectra and simultaneously we have also measured the photoluminescence (PL, SYNERGY MX BIOTEK). The scanning electron microscopy (SEM) (HITACHI S-3400 N), field emission SEM (ULTRA^{TM} 55 UK ZEISS) and high resolution transmission electron microscopy (HRTEM) (FEI TECHNAI G^2 200 kV S-twin) to study the shape and size and morphology of the particles. Differential scanning calorimetry (DSC TA instruments) and TGA (TA instruments) were performed for the phase transformation. Elemental analysis was performed by the energy dispersive X-ray spectroscopy (EDS) (HORIBA X-ray). IR-active vibrational characteristics were revealed by Fourier transform infra-red (FT-IR) (Nicolet model Impact-410), Raman spectroscopy was studied using the Micro-Raman (LabRam HR800 Raman Spectrometer, HORIBA Jobin Yvon). The emission spectrum was acquired and simultaneously we investigated the photoluminescence (PL) (option with a plate reader, SYNERGY MX BIOTEK). The three dimensional structures were confirmed by atomic force microscopy (SII Oo Seiko Instruments Inc.) study and Electron paramagnetic resonance behaviour were (Bruker WIN-EPR Bruker).

Results and discussion

Variation of shape and size of the ZnO have been controlled with surfactant concentrations. We chose six different concentrations of surfactant such as 0.05, 0.10, 0.50, 0.75 and 1.0ml. Six sets weight of precursor and six sets volume of water were taken separately. When surfactant concentration was 0.05ml, hexagonal shaped (disk shaped) nanoparticles were formed. They are found to be quite uniform in shape and size. The geometrical parameters of the spherical hexagonal shaped particles are calculated and found to be a=40nm, b=40nm, c=46nm, **(Fig. 1)** which match well with the SEM results for the corresponding sample. On increasing the concentration of surfactant the ZnO NPs particles were converted into the rod shape and the length of the rod increased up to a certain length.

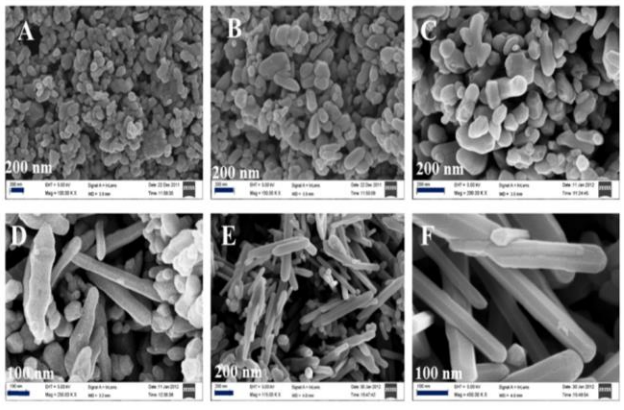

Fig. 1. FESEM micrographs of ZnO nanorods/nanoparticles, (A) S6 (nanoparticles), (B) S5, (C) S4, (D) S3, (E) S2 and (F) S1 (nanorods) of lower to higher aspect ratio, respectively.

Fig. 1A to **1F** show the shape of ZnO nanoparticles obtained at different concentrations. Likewise, the shape and size of the nanoparticles are investigated by SEM and shown in **Fig. 1A** at 0.05 mL (S6), **Fig. 1B** at 0.1ml (S5), **Fig. 1C** at 0.25 ml (S4), Fig. 1D at 0.5ml (S3), Fig. 1E at 0.75mL (S2) and Fig. 1F at 1.0ml (S1) surfactant, respectively. It is worth mentioning that sample S1 for long rod particles and sample S6 is for disk shaped nanoparticles and length of the nanoparticles increased from S6 to S1 as the concentrations of Igapal CO50 have been changed.

Further detailed information on the shape, size and morphology was obtained from HRTEM results. It was found that at 0.05ml surfactant concentration, only hexagonal shaped nanoparticles were formed (Fig. 1 S6) with the geometrical parameters of a=40 nm, b=40 nm, c=46 nm **(Fig. 2a)** which matched well with the FESEM results. To investigate the lattice arrangements and the crystal structure, high magnified images and SAED pattern were acquired **(inset of Fig. 2a).** It was found that the lattice spacing is ~4.44Å and the crystal structure is hexagonal in nature. Similar results have also been confirmed through the AFM analysis (supporting file**, Fig. S1).**

The HRTEM observation revealed that the ZnO nanorods are formed at higher concentration (1.0ml surfactant) (sample S1) and at lower concentration of surfactants (0.05ml surfactant) nanoparticles of lower aspect ratio has been formed (sample S6) which is agreed well with the FESEM results. At this concentration hexagonal shaped nanoparticles are formed and they are mono dispersed. Further, the nanorods formed are well dispersed and separated from each other **(Fig. 2b)** and their "a" and "b" structural parameters are equal to the dimension of "a" and "b" of sample S1. This means the one-dimensional growth of the particle occurs preferably. The aspect ratio of the ZnO NPs increased from S6 to S1 with increase in the Igapal CO50 concentration. As example, at 1.0 ml Igapal CO50 concentration nanorod obtained are of size 300-450 nm with 60-80 nm width **(Fig. 2b)** which matches well with FESEM results **(Fig. 1).** Crystalline 'd' spacing for the nanorods has found to be 4.45Å. The three-dimensional (3D) information for the ZnO nanoparticles and rods were confirmed by AFM analysis **(Fig. S2)** and the results match well with the HRTEM and FESEM results. When the ZnO nanoparticles were synthesized with 0.5 mL Igapal CO 50, a mixture of rods of short length and spherical particles were formed **(Fig. S3).** However, from the microscopy results it is clear that the particles changed from disk to 3D nanoparticles and then into the rods.

However, some of the ZnO nanorods look like core shell structure **(Fig. S4).** The reason might be the difference in the concentration of O in ZnO nanoparticles which will be further investigated and it is not in the scope of the present study.

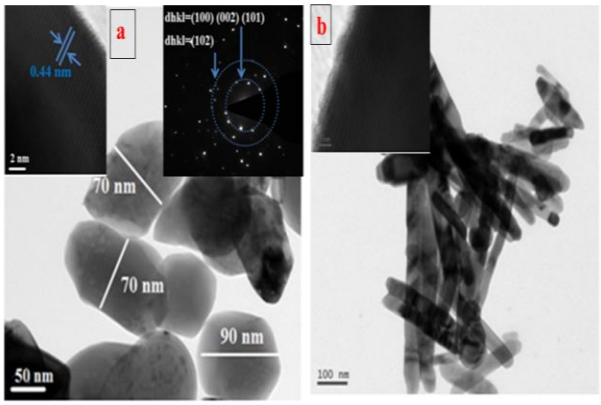

Fig. 2. HRTEM images of ZnO nanoparticles (S6) (inset lattice d spacing and SAED pattern) (b) ZnO nanorods (S1).

XRD analysis of ZnO nanoparticles/ nanorods/core shell nanorods

The XRD patterns of ZnO nanoparticle are shown in **Fig. 3(a)**. ZnO exhibits two main crystal forms, hexagonal wurtzite and cubic zinc blende **[17–19].** The wurtzite structure is most stable at ambient conditions and thus the most common form. In our samples, ZnO nanorods/ particles exhibit hexagonal crystal structure, which is characterized by prominent peaks at 2θ = 31.9, 34.6, 36.5, 47.7, 56.8, 63.0, 66.5, 68.2, 72.8, 77.1 and 81.6, corresponding to the preferred orientations of (100), (002), (101), (102), (110), (103), (200), (112), (201), (004) and (202) diffraction planes, respectively. The appearance of prominent peaks with respect to Bragg's angles (2θ) is consistent and matching with the earlier reports of the ZnO systems **[20, 21].** Any supplementary peaks correspond to the other oxide forms of Zn (e.g., ZnO_2, Zn_2O, etc.) or can be the residues of Igapal CO 50 are not observed.

Table 2. Physical parameters of the various synthesized ZnO nanoparticles/rods calculated from XRD.

Nanomaterials at different concentration of surfactant	Lattice parameter (Å)	Micro-strain	Crystallite size (nm)
ZnO nanorods (1.0ml) , (S1)	a=3.143 b=3.143 c=5.117	1.13×10^{-3}	17
ZnO nanorods+particles (0.75 ml), (S2)	a=3.243 b=3.243 c=5.195	1.12×10^{-3}	19
ZnO nanorods+particles (0.50ml), (S3)	a=3.243 b=3.243 c=5.195	1.27×10^{-3}	24
ZnO nanorods+particles (0.25ml), (S4)	a=3.243 b=3.243 c=5.195	1.32×10^{-3}	21
ZnO nanorods+particles (0.10ml), (S5)	a=3.243 b=3.243 c=5.195	1.38×10^{-3}	26
ZnO nanoparticles (0.05ml), (S6)	a=3.243 b=3.243 c=5.195	1.42×10^{-3}	30

The lattice parameter, average crystallite size and microstrain are also calculated and listed in **Table 2**. They were calculated using the Williamson-Hall model (eq^n. 1) **[22]**:

$$\beta\text{Cos}\theta = 0.9\lambda/l + 4\varepsilon\ \text{Sin}\theta \quad \text{(eq}^n\text{. 1)}$$

where, β is the full width at half maxima (FWHM), λ is the wavelength of X-rays (Cu, K_α=1.543 Å), ε is the microstrain and *l* is the average crystallite size. The estimated lattice parameters of ZnO nanorods and nanoparticles (Table 2) are found to be in good agreement with the reported results **[21, 23, 24]**. The lattice parameters for ZnO samples prepared at surfactant concentration 0.05ml (S6), 0.10ml (S5), 0.250ml (S 3), 0.50ml (S 4), and 0.75ml (S5) are remained unchanged (a=3.243Å, b=3.243Å, c=5.195Å), whereas, same values for ZnO nanorods synthesized at surfactant concentration of 1.0ml (S1) have been varied and found to be a=3.14Å, b=3.14Å, and c=5.12Å, respectively. Further, it is found that as the surfactant concentration increases from 0.05ml (S6) to 1.0ml (S1), the microstrain of the crystal gradually decreases from 1.38×10^{-3} to 1.13×10^{-3} and the crystallite size gradually decreases from 26 nm to 17nm.

EDS analysis of ZnO nanoparticles /nanorod /core shell nanorods

EDS response of ZnO nanoparticles/nanorods which exhibited sharp peaks correspond to zinc and oxygen atoms as main elements. The absence of other trace elements ensured the high purity of the synthesized products for all the ZnO samples. It is observed that the elemental percentage of Zn (weight %) and atomic % are increased with a decrease in the concentration of surfactant. It may be due to the presence of the elemental zinc in the samples which are not converted into zinc oxide. The EDS spectra of all the ZnO samples prepared at different concentration of surfactant are shown in supporting **Fig. S5.**

DSC and TGA study of ZnO nanoparticles /nanorods/ core shell nanorods

The differential scanning calorimetric studies of the prepared ZnO nanoparticles were performed at low temperatures to study the transition temperature for phase change. The DSC thermogram of ZnO nanoparticles are shown in Figure S6. We found that only one endothermic peak at 150ºC is appeared which means all the samples are in the pure form of ZnO and no other phases of ZnO are formed during synthesis.

Further to check the purity TGA experiments were performed for various ZnO sample **(Fig. S7).** It is obvious from Fig. S7 that there is no prominent weight loss for all the samples occurred. Only 2% weight loss is observed around 100 ºC which is due to the presence of moisture.

Spectroscopy analysis of ZnO nanoparticles

Raman active modes of ZnO samples having various size and shape have been shown in **Fig. S8**. The crystal structure of ZnO samples are wurtzite hexagonal types and belong to the $P6_3$ */mmc* (C^4_{6v}) space group. Crystal primitive unit cell of ZnO forms with two formula units where all the atoms occupy the C_{3v} sites **[25]**. Zone centre optical phonon interactions of ZnO sample can be predicted from the group theory: $A_1+ 2E_2+ E_1$. Among these three phonon modes, A_1 and E_2 symmetry are polar and exhibited different frequencies for transverse-optic (TO) and longitudinal-optic (LO) **[26]**.

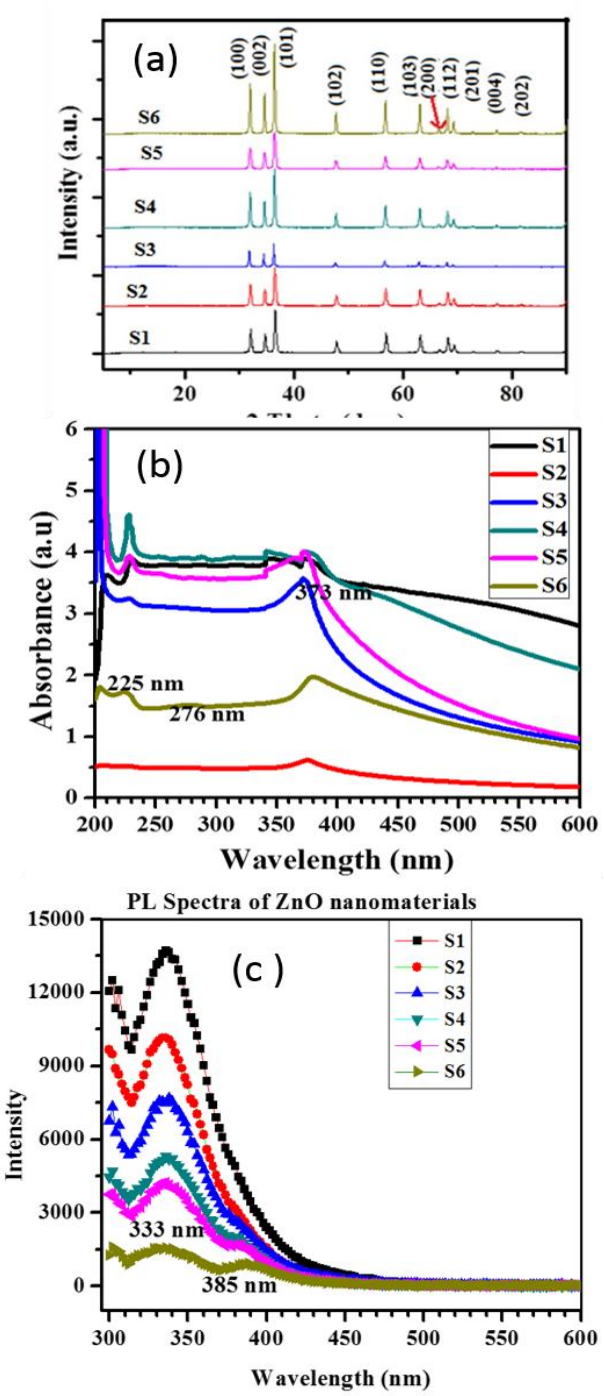

Fig. 3. (a) X-ray diffraction pattern of various ZnO samples with their different aspect ratio, **(b)** UV-Visible NIR absorption spectra of ZnO samples with different aspect ratio. **(c)** Photoluminescence spectra of various ZnO samples with different aspect ratio.

All the spectra for different ZnO samples can be explained by seven well-developed peaks, corresponding to transverse optic (TO) and longitudinal optic (LO) modes, which are observable at 329.4, 436.0, 509.6, 657.7, 992.4, 1033.7 and 1331.2 cm^{-1}, respectively **[25–32]**. The 329.4 cm^{-1} mode could be observed by enhancement of Raman active and inactive phonons with lattice symmetry due to disorder-activated Raman scattering (DARS) **[33]**. In addition, the Raman band is observed at around the "M" point of the Brillouin zone **[34]**. There is a possibility of phonon confinement due to the differences in sizes and shape of the ZnO particles.

However, for all the ZnO samples, no variation in band positions was observed due to the unaltered nature of the phases and they are not structurally modified other than the change in the defective levels which caused the change in the surface polarization.

UV-Vis spectra are shown in **Fig. 3(b)** for different ZnO samples having different aspect ratio. The UV-Vis spectra of the all ZnO samples were performed at room temperature. An absorption peak at 373 nm for them is obtained. An absorption peak at 373 nm for the anisotropic ZnO is blue shifted as compared to the ZnO nanorods. Additional absorption peaks at 225 and 276 nm are observed for the defect structure of ZnO. The blue shift of the absorption bands for the ZnO nanoparticles (sample S6) compared to the ZnO nanorods (sample S6) occurs due to the optical phonon confinement by nanostructures and/or the phonon localization by O^{-2} defects, and/or due to the anisotropic internal strains corresponding to the different growth directions **[35,36]**. This is a consequence of the confinement of the suspended delocalization of in-plane electrons, which leads to a significant blue shift in the electron spin resonance band in ZnO sample.

Fig. 3(c) shows the photoluminescence (PL) spectra for ZnO samples synthesized at different concentrations of the surfactant. First, ZnO nanoparticles were dispersed in isopropanol through sonication. We collected the PL spectra at 270 nm excitation wave length for all the samples. From **Fig. 3(c),** it is obvious that a strong emission peak was observed at 333 nm for all the samples, whereas the samples prepared at 0.05 (S6), 0.1 (S5) and 0.25ml (S4) surfactant concentration are showing an additional peak at ~385 nm wavelength. However, the peak that appeared at 333nm for 0.05ml surfactant is quite prominent and separate from the peak observed at 333nm. The peak that appears at 385nm wavelength is due to the large oxygen vacancy present in ZnO nanostructure. The oxygen creates deep level vacancies (V_o) and can trap one or two electrons (V_o^+) **[31, 33]**. It was also observed that as the surfactant concentration increases the intensity of the peak appeared at 385 nm diminished gradually which is related to the defect levels of the ZnO. Furthermore, due to the grain growth of the ZnO from nanoparticles to nanorods, a large number of structural defects have been compromised through the deposition of nucleates and rearrangement of the structure with multiple transition **[37].** Growth of the particles further helps to trap the oxygen defects present on the surface of the particles. The rate for a surface trapping process decreases as the nanoparticle changes into the nanorods since the free surface-to-volume ratio decreases at constant mass **[38,39].** All these are the impact of the surface interaction of ZnO particles with the living cells and it has been discussed in the subsequent section.

Biomedical applications of ZnO nanoparticles

Cytotoxicity of different ZnO nanoparticle

Cytotoxicity of different ZnO samples have been investigated in cell based *in-vitro* systems (Fig. 4). In PBS medium, both the ZnO nanoparticles and lymphocyte cells (normal blood cell) tend to form aggregates. The ZnO nanoparticles appeared to display normal cell activities as a result of cell death. The ZnO nanoparticles tend to conjugate with lymphocyte due to the physical and surface chemical interactions. For our experiment, 5000 cells were incubated with various concentrations of ZnO nanoparticles. Toxicity was evaluated by measuring the optical density of solution containing both the cells and ZnO nanoparticles. It is reported that these materials are very less toxic against the normal cells **[19,40,41].**

To determine the usefulness in medical biotechnology, cytotoxicity of the ZnO nanoparticles/ nanorods was investigated. The normal lymphocyte cells and chronic myeloid leukemia cancer cells (K562) were incubated at different concentrations of the sample (e.g., 50, 100, 200, 400 and 500 mg ml^{-1}) according to our standard protocol. The results **(Fig. 4)** showed that more than 22% of the cells are inhibited after 24 h of incubation at the maximum concentration of ZnO 'nanoparticle/ nanorods **(Fig 4).** Furthermore, it is observed that the inhibition rate is higher for the smaller sized (low aspect ratio) ZnO NPs. However, as the aspect ratio of ZnO NPs gradually increases, the inhibition rate on the cancer cells found decreases. For the bare ZnO nanoparticles, inhibition rate is higher for nanoparticles and lower for the nanorods. Since the surface area to volume ratio is more for NPs, the inhibition rate is higher for NPs. As the surface area to volume ratio increases, the extent of O^{-2} defects also increases, which we have observed from the UV-Vis (**Fig. 3(b))** and PL (**Fig. 3(c)**) results.

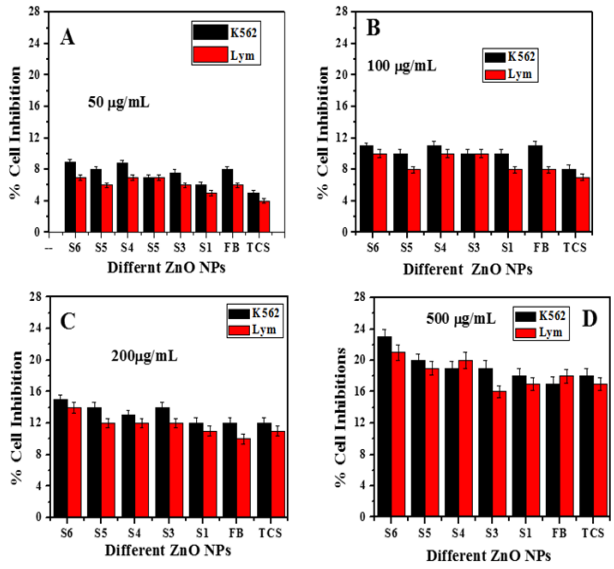

Fig. 4. Cell Inhibition of lymphocyte cell growth and carcinoma cell growth (K562) by ZnO nanoparticles/nanorods at various concentrations of (a) 50 µg/mL, (b) 100 µg/mL, (c) 200 µg/mL, and (d) 500 µg/mL, respectively.

More defective sites of ZnO exhibited more effective interactions with living cells (Fig. 4). Furthermore, it is also observed that the inhibition effects on cancer cells (K562) are much higher compared to the normal cells (lymphocyte cell).

To check the possible reasons for the interaction of the ZnO NPs with cells, the EPR have been performed at

room temperature **(Fig. 5)**. This interaction study was performed based on the particles size (aspect ratio) of ZnO samples. Since the different ZnO NPs have different extent of defective levels, the electronic environment and the magnetic moment of the O^{-2} are different for different shapes and sizes of the particles. ZnO NRs (high aspect ratio) are confined due to the directional growth of ZnO along the c-axis, whereas the ZnO NPs with same mass have overall huge defect states. From **Fig. 5**, it is obvious that there are possibilities of limited interactions (less point of contact on the cell surface) of the NRs surface with water molecules on the cell wall and less defects due to the less surface area to volume ratio, and hence produce a smaller extent of free radicals or singlet oxygen in a cell-water suspension and is supposed to produce less intense EPR peaks compared to the ZnO NRs having high aspect ratio (sample S6). And as the aspect ratio of ZnO NRs increases, the EPR intensity also decreases, due to the less paramagnetic defective oxygen. Thus, EPR study **(Fig. 5 a and b)** also indirectly reveals that when ZnO nanoparticles are incubated with the cells, there is a huge possibility of charge or electron transfer from the ZnO nanoparticles to the cells due to the difference in the moment of paramagnetic electrons which is more for ZnO nanoparticles (sample S6) compared to the ZnO NRs having high aspect ratio (sample S5 →S1). Similar interaction results were observed in our earlier study, where the ZnO NPs's surface was capped with a layer of SiO_2 and produced fewer free radicals due to the limited interaction with water. The intensity of EPR peak and cell viability of triangular core-shell nanoparticles were low compared to the bare ZnO nanoparticles, possibly due to the confinement of defective oxygen inside the SiO_2 core **[19,41]**. Earlier we found that the paramagnetic behavior of assembled ZnO '*dandelions*' capsules is moderate compared to the ZnO NPs, since they are formed with the self-assembly of ZnO NPs and NRs with high aspect ratios. The effect on cancer cells is less compared to the ZnO NPs of low aspect ratio (~1.3). The interaction with cancer cells is also less compared to the ZnO NPs **[40]**.

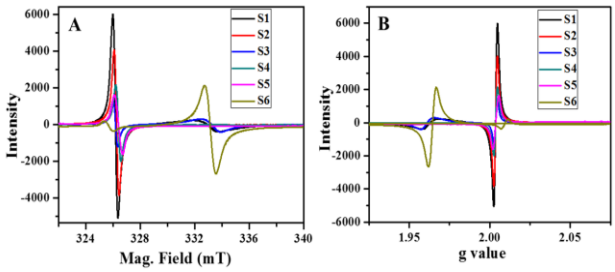

Fig. 5. EPR spectra (a) magnetic field vs. Intensity and (b) g value vs. Intensity of ZnO samples with different aspect ratio.

Further, the difference in cell interaction with different ZnO NPs is observed, and can also be explained by the EPR (**Fig. 5**). Due to the anisotropy of the particle size and shape of ZnO, the overall angular momentum and spin-orbital coupling are different. Therefore, the electron spin alignment occurs at the different effective magnetic field strength (B_o) in the resonance conditions, which is further associated with the extent of defects of oxygen level in the structure and such the cell killing capacity is different and changes with the aspect ratio of ZnO nanoparticles. Furthermore, Raman bands (Fig. S8) appeared in different ZnO samples due to the phonon localization of oxygen defects (V_o^+), which is also related to the anisotropic internal strains corresponding to the directional crystal growth along c-direction of the unit cell **[1,9]**. Depending on the direction and the extent of growth, the paramagnetic behavior is actually different **(Fig. 5).** It is higher for ZnO NPs (sample 1) with smaller aspect ratio and maximum defects (V_o^+) and it enhanced the efficiency of interaction with the living cells compared to the ZnO NRs (S5→S6). Due to all these reasons, ZnO nanoparticles with smaller aspect ratios are much more efficient in killing the cancer cells compared to the ZnO nanoparticles with high aspect ratios, i.e., nano rods etc.

Conclusion

In summary, this work emphasized on the toxicity, shape, size and morphologies of the ZnO NPs. The synthesis strategies, and surface morphology of ZnO nanoparticles, have been studied. It has been found that the size and shape of the ZnO varies with concentration of surfactant. It is worth mentioning that the different synthesis routes produce different structures. However, by changing with single parameter during the synthesis will have better control on the size, shape, morphology, physical properties and interactions with living cells are of the great interest to tune the biological activities and applications in the medical field. Size and shape dependent interactions were investigated with Lymphocytes normal cells and with K562 a (Leukaemia cancer Cells) through MTT assay without loading of anticancer drugs and manifests that the size, shape and physical properties of ZnO are preferentially the critical factors in interactions and killing of the cancer cells. This phenomenon has been explained on the basis of oxygen defects and on the electron paramagnetic behaviors which strongly control the rate of production of oxygen radicals or singlet oxygen on the cell surface of carcinoma cells. Depending on the extent of production of oxygen radicals or singlet oxygen ZnO NPs with low aspect ratio is more vigorous to kill the carcinoma cells compared to the ZnO with higher aspect ratio. Results of this study direct us to select ZnO nanoparticles with exact aspect ratio to tune the biological activity in exact extent.

Acknowledgements

Authors acknowledge the financial support from the Department of Sciences and Technology (DST) Fast-Track Grant for Young Scientist (Ref: SR/FTP/ETA-0079/2011) and UOH START-Of-GRANT (Ref: UH/F&A/2011-12/SG), School of Life Sciences, UOH for cell culture facilities and for related biological studies.

References

1. Chen, C.; Liu, P.; Lu, C. *Chem. Eng. J.* **2008**, *144* (3), 509. **DOI:** 10.1016/j.cej.2008.07.047
2. Papavlassopoulos, H.; Mishra, Y. K.; Kaps, S.; Paulowicz, I.; Abdelaziz, R.; Elbahri, M.; Maser, E.; Adelung, R.; Röhl, C. *PLoS One* **2014**, *9* (1), e84983.

DOI: 10.1371/journal.pone.008498
3. Sruthi, S.; Mohanan, P. V. *Colloids Surfaces B Biointerfaces* **2015**, *133*, 1. **DOI:** 10.1016/j.colsurfb.2015.05.041
4. Kang, T.; Guan, R.; Chen, X.; Song, Y. *Nanoscale Res.* **2013**, *8*, 496. **DOI:** 10.1186/1556-276X-8-496
5. Churchman, A. H.; Wallace, R.; Milne, S. J.; Brown, A. P.; Brydson, R.; Beales, P. A. *Chem. Commun. (Camb).* **2013**, *49* (39), 4172. **DOI:** 10.1039/c3cc37871c
6. Moos, P. J.; Chung, K.; Woessner, D.; Honeggar, M.; Cutler, N. S.; Veranth, J. M. *Chem. Res. Toxicol.* **2010**, *23* (4), 733. **DOI:** 10.1021/tx900203v
7. Hanley, C.; Layne, J.; Punnoose, A.; Reddy, K. M.; Coombs, I.; Coombs, A.; Feris, K.; Wingett, D. *Nanotechnology* **2008**, *19* (29), 295103. **DOI:** 10.1088/0957-4484/19/29/29510
8. Ashutosh Tiwari, Y.K. Mishra, H. Kobayashi, A.P.F. Turner (Eds), In the Intelligent Nanomaterials, 2nd Edition, John Wiley & Sons, USA, **2016**.
9. Yang, J. H.; Zheng, J. H.; Zhai, H. J.; Yang, L. L.; Zhang, Y. J.; Lang, J. H.; Gao, M. *J. Alloys Compd.* **2009**, *475*, 741. **DOI:** 10.1016/j.jallcom.2008.07.123
10. Li, M.-K.; Wang, D.-Z.; Ding, S.; Ding, Y.-W.; Liu, J.; Liu, Z.-B. *Appl. Surf. Sci.* **2007**, *253* (9), 4161. **DOI:** 10.1016/j.apsusc.2006.09.019
11. Komarneni, S.; Bruno, M.; Mariani, E. *Mater. Res. Bull.* **2000**, *35*, 1843. **DOI:** 10.1016/S0025-5408(00)00385-8
12. Lee, E. T. Y.; Shimotsuma, Y.; Sakakura, M.; Nishi, M.; Miura, K.; Hirao, K. *Mater. Lett.* **2008**, *62* (24), 4044. **DOI:** 10.1016/j.matlet.2008.05.066
13. Cho, S.; Jung, S.-H.; Lee, K.-H. *J. Phys. Chem. C* **2008**, *112 (33)*, 12769. **DOI:** 10.1021/jp803783s
14. Sirelkhatim, A.; Mahmud, S. *J. Nanoparticle Res.* **2016**, *18* (219), 1. **DOI:** 10.1007/s11051-016-3531-x
15. Cai, X.; Luo, Y.; Zhang, W.; Du, D.; Lin, Y. *ACS Appl. Mater. Interfaces* **2016**, *8*, 22442. **DOI:** 10.1021/acsami.6b04933
16. Sirelkhatim, A.; Mahmud, S.; Seeni, A.; Kaus, N. H. M.; Ann, L. C.; Bakhori, S. K. M.; Hasan, H.; Mohamad, D. *Nano-Micro Lett.* **2015**, *7* (3), 219. **DOI:** 10.1007/s40820-015-0040-x
17. Songjun Li, Yi Ge, Ashutosh Tiwari, Shunsheng Cao (Eds), In the A Temperature-Responsive Nanoreactor, WILEY-VCH Verlag, USA, **2010**.
18. Ding, Y.; Wang, Z. L.; Sun, T.; Qiu, J. *Appl. Phys. Lett.* **2007**, *90* (15), 153510. **DOI:** 10.1063/1.2722671
19. Kumar, V. B.; Annamanedi, M.; Prashad, M. D.; Arunasree, K. M.; Mastai, Y.; Gedanken, A.; Paik, P. *J. Nanoparticle Res.* **2013**, *15* (9), 1904. **DOI:** 10.1007/s11051-013-1904-y
20. Zhou, T.; Lu, M.; Zhang, Z.; Gong, H.; Chin, W. S.; Liu, B. *Adv. Mater.* **2010**, *22* (3), 403. **DOI:** 10.1002/adma.200901801
21. Azam, A.; Ahmed, F.; Arshi, N.; Chaman, M.; Naqvi, A. H. *J. Alloys Compd.* **2010**, *496* (1–2), 399. **DOI:** 10.1016/j.jallcom.2010.02.028
22. Williamson, G. K.; Hall, W. H. *Acta Metall.* **1953**, *1*, 22. **DOI:** 10.1016/0001-6160(53)90006-6
23. Liu, X.; Zhang, J.; Wang, L.; Yang, T.; Guo, X.; Wu, S.; Wang, S. *J. Mater. Chem.* **2011**, *21* (2), 349. **DOI:** 10.1039/c0jm01800g
24. Atul Tiwari, Ashutosh Tiwari (Eds), Bioengineered Nanomaterials, CRC Press, USA, **2013**.
25. Farhat, O. F.; Halim, M. M.; Abdullah, M. J.; Ali, M. K. M.; Allam, N. K. *Beilstein J. Nanotechnol.* **2015**, *6*, 720. **DOI:** 10.3762/bjnano.6.73
26. Pal, U.; Serrano, J. G.; Santiago, P.; Xiong, G.; Ucer, K. B.; Williams, R. T. *Opt. Mater. (Amst).* **2006**, *29* (1), 65. **DOI:** 10.1016/j.optmat.2006.03.015
27. Musić, S.; Dragčević, D.; Popović, S.; Ivanda, M. *Mater. Lett.* **2005**, *59* (3), 2388. **DOI:** 10.1016/j.matlet.2005.02.084
28. Ashutosh Tiwari, Atul Tiwari (Eds), In the Nanomaterials in Drug Delivery, Imaging, and Tissue Engineering, John Wiley & Sons, USA, **2013**.
29. Manjón, F. J.; Marí, B.; Serrano, J.; Romero, a. H. *J. Appl. Phys.* **2005**, *97* (5), 1. **DOI:** 10.1063/1.1856222
30. Alim, K. a.; Fonoberov, V. a.; Shamsa, M.; Balandin, A. a. *J. Appl. Phys.* **2005**, *97* (12), 1. **DOI:** 10.1063/1.1944222
31. Tang, Q.; Zhou, W.; Shen, J.; Zhang, W.; Kong, L.; Qian, Y. *Chem. Commun. (Camb).* **2004**, *1* (6), 712. **DOI:** 10.1039/b313387g
32. Kumar, P. S.; Paik, P.; Raj, A. D.; Mangalaraj, D.; Nataraj, D.; Gedanken, A.; Ramakrishna, S. *Appl. Surf. Sci.* **2012**, *258* (18), 6765. **DOI:** 10.1016/j.apsusc.2012.03.051
33. Mead, D. G.; Wilkinson, G. R. *J. Raman Spectrosc.* **1977**, *6* (3), 123. **DOI:** 10.1002/jrs.1250060305
34. Serrano, J.; Romero, a.; Manjón, F.; Lauck, R.; Cardona, M.; Rubio, a. *Phys. Rev. B* **2004**, *69* (9), 1. **DOI:** 10.1103/PhysRevB.69.094306
35. Brus, L. *J. Phys. Chem.* **1986**, *90* (12), 2555. **DOI:** 10.1021/j100403a003
36. Wang, Y.; Herron, N. *J. Phys. Chem.* **1991**, *95* (2), 525. **DOI:** 10.1021/j100155a009
37. Tiwari, A.; Tiwari, A.(Eds), John Wiley & Sons, USA, **2012**.
38. Van Dijken, a.; Meulenkamp, E. a.; Vanmaekelbergh, D.; Meijerink, a. *J. Lumin.* **2000**, *87*, 454. **DOI:** 10.1016/S0022-2313(99)00482-2
39. Schoenmakers, G. H.; Vanmaekelbergh, D.; Kelly, J. J. *J. Phys. Chem.* **1996**, *100* (8), 3215. **DOI:** 10.1021/jp952392f
40. Kumar, V. B.; Kumar, K.; Gedanken, A.; Paik, P. *J. Mater. Chem. B* **2014**, *2* (25), 3956. **DOI:** 10.1039/c4tb00416g
41. Kumar, V. B.; Gedanken, A.; Paik, P. *ChemPhysChem* **2013**, *14* (14), 3215. **DOI:** 10.1002/cphc.201300480

Supplementary information

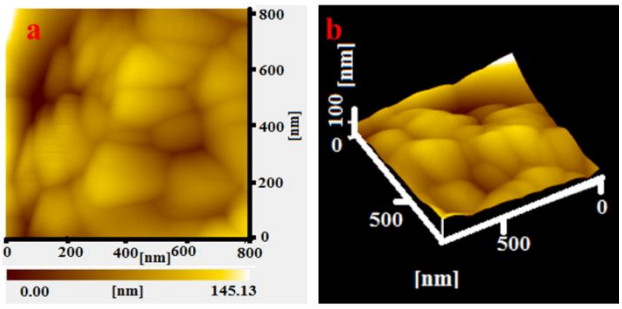

Fig. S1. AFM images of ZnO nanoparticles (0.05ml surfactant) (a) topography images (b) 3D view of the same.

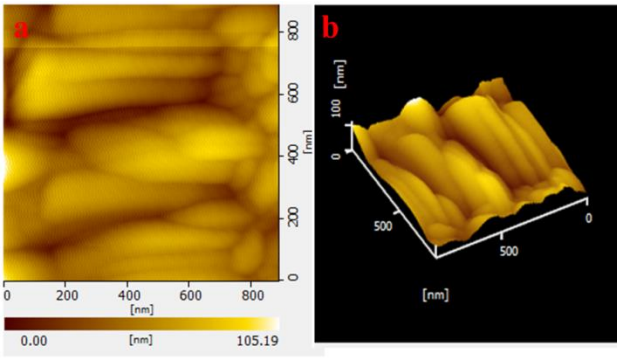

Fig. S2. AFM images of ZnO nanoparticles (0.05ml surfactant) (a) topography images (b) 3D view of the same.

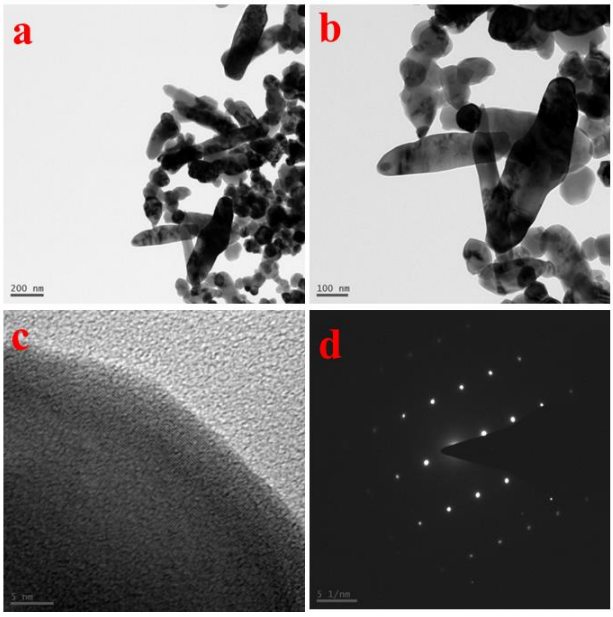

Fig. S3. TEM images of ZnO nanoparticles (0.5ml surfactant)) (a and b) at lower magnification (c) at higher magnification (d) SAED pattern of the same.

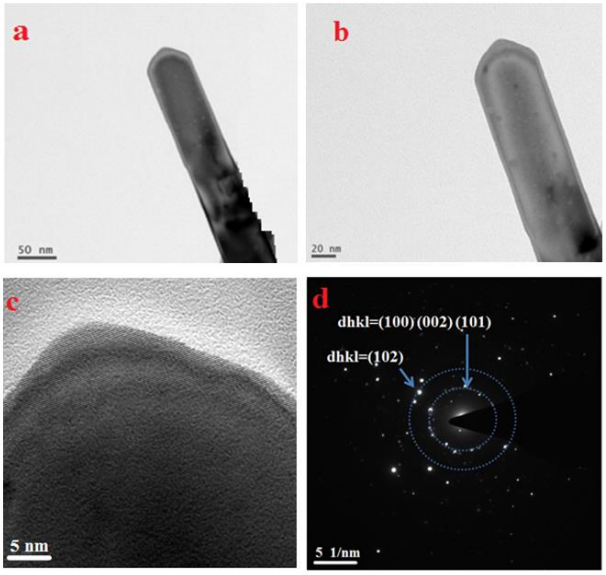

Fig. S4. HRTEM images of ZnO core shell nanoparticles (0.75ml surfactant)) (a and b) at lower magnification (c) at higher magnification (d) SAED pattern of ZnO core shell nanoparticles.

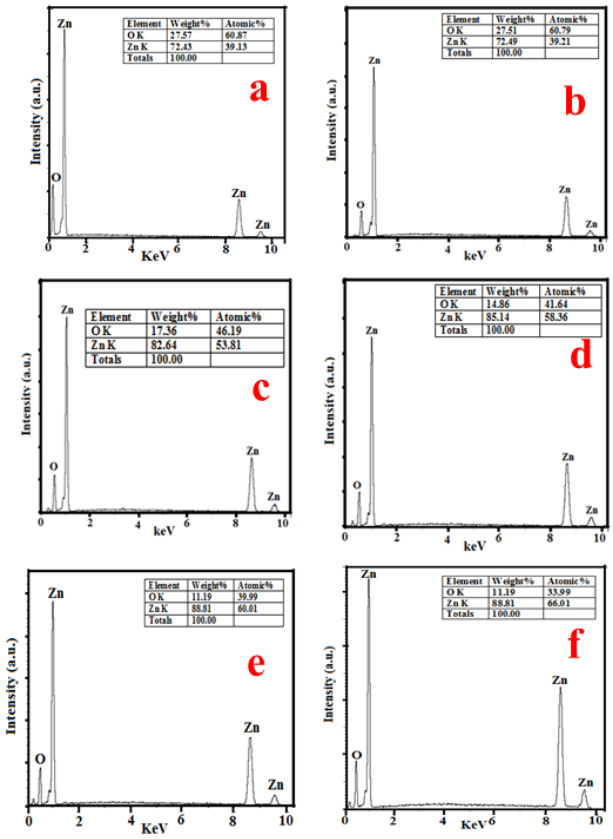

Fig. S5. (a) EDS spectra of ZnO nanorods (1.0ml surfactant) (b) EDS spectra of ZnO nanoparticles/rods (0.75ml surfactant) (c).EDS spectra of ZnO nanoparticles/rods (0.5ml surfactant) (d) EDS spectra of ZnO nanoparticles/rods (0.25ml surfactant) (e) EDS spectra of ZnO nanoparticles/rods (0.10ml surfactant) (f) EDS spectra of ZnO nanoparticles (0.05ml surfactant).

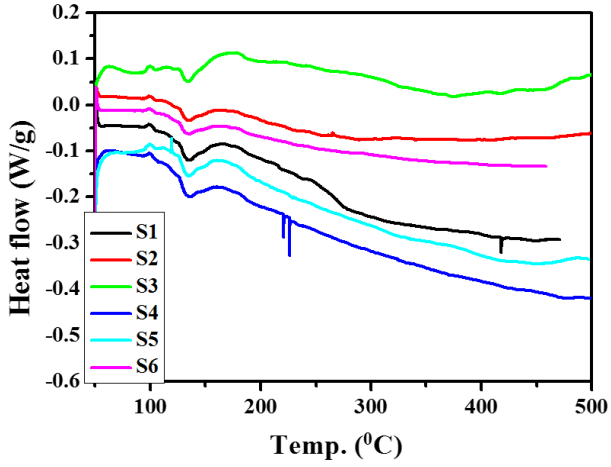

Fig. S6. DSC thermogram of ZnO nanoparticle/nanorods/ZnO nanorods having different aspect ratio.

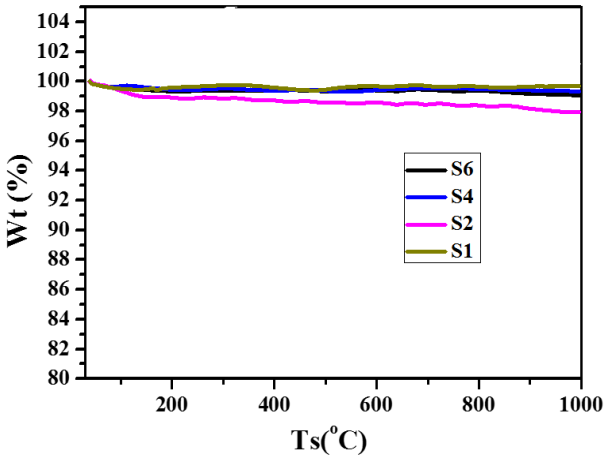

Fig. S7. TGA thermogram of various ZnO samples having different aspect ratio.

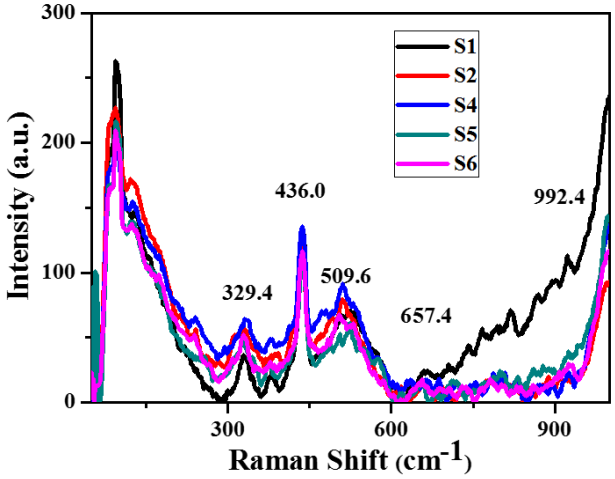

Fig. S8. Raman Spectra of ZnO samples with different aspect ratio.